MDPI

Article

Influence of Lithium-Ion-Battery Equivalent Circuit Model Parameter Dependencies and Architectures on the Predicted Heat Generation in Real-Life Drive Cycles

Marcus Auch [1],*, Timo Kuthada [2], Sascha Giese [1] and Andreas Wagner [1]

[1] Institute of Automotive Engineering (IFS), University of Stuttgart, 70569 Stuttgart, Germany
[2] Research Institute for Automotive Engineering and Vehicle Powertrain Systems Stuttgart (FKFS), 70569 Stuttgart, Germany
* Correspondence: marcus.auch@ifs.uni-stuttgart.de

Abstract: This study investigates the influence of the considered Electric Equivalent Circuit Model (ECM) parameter dependencies and architectures on the predicted heat generation rate by using the Bernardi equation. For this purpose, the whole workflow, from the cell characterization tests to the cell parameter identification and finally validation studies, is examined on a cylindrical 5 Ah LG217000 Lithium-Ion-Battery (LIB) with a nickel manganese cobalt chemistry. Additionally, different test procedures are compared with respect to their result quality. For the parameter identification, a Matlab tool is developed enabling the user to generate all necessary ECMs in one run. The accuracy of the developed ECMs is evaluated by comparing voltage prediction of the experimental and simulation results for the highly dynamic World harmonized Light vehicle Test Cycle (WLTC) at different states of charges (SOCs) and ambient temperatures. The results show that parameter dependencies such as hysteresis and current are neglectable, if only the voltage results are compared. Considering the heat generation prediction, however, the neglection can result in mispredictions of up to 9% (current) or 22% (hysteresis) and hence should not be neglected. Concluding the voltage and heat generation results, this study recommends using a Dual Polarization (DP) or Thevenin ECM considering all parameter dependencies except for the charge/discharge current dependency for thermal modeling of LIBs.

1. Introduction

In June 2022, the European Union played a leading role in the fight against climate change by proclaiming the prohibition of the registration of new internal combustion engines from 2035 going forward (except e-fuels) [1]. Battery electric vehicles (BEVs) have already established themselves in the market and are likely to become the main powertrain technology in the near future. Hence, battery power-train applications have become one of the most important topics in engineering research.

Currently, Lithium-Ion-Batteries (LIB) are the main choice for application in BEVs, because of their high power density, energy density, low self-discharge rate and long service life [2]. However, for application in BEVs, thermal safety and degradation of LIBs are two of the most challenging topics [3]. It has been widely studied that capacity, cycle life and safety are highly dependent on the LIB temperature [4–6]. According to Pesaran [7], the optimum operating temperature of LIBs is between 25–40 °C. Lower and higher temperatures result in degradation [6]. Operating the LIB at lower temperatures results in capacity reduction due to lithium plating. On the other hand, higher temperatures lead to degradation due to the faster growth of the solid electrolyte interphase (SEI) layer or can even result in a thermal runaway scenario of the LIB.

This leads to the topic of this research paper: the heat generation prediction of cylindrical battery cells for the application in BEVs. For an accurate design of the thermal management, reliable models are necessary to describe the generated heat while operating the LIBs. Hence, models are used to capture the electrical and thermal behavior of LIBs. These models estimate the State of Charge (SOC), State of Health (SOH), heat generation $\dot{Q}$, available power and available energy of a battery cell [8].

According to Nejad [9], there are three common modeling methodologies for battery cells. Firstly, there are the electrochemical or physic-based models, the Single-Particle Model; Pseudo 2D Model; second, empirical or data driven models [10] and lastly the Equivalent Electrical Circuit Models (Rint-Model and Thevenin-Model). As already indicated by the name, physics-based models are based on the detailed electrochemical understanding of the cell's operation and dynamic. This behavior is determined by physical equations describing the processes and reactions occurring in the battery cell. Data driven models and Equivalent Circuit Models (ECM) do not need a detailed understanding of the electrochemical processes. Data driven models rely on generated training data and hence need a lot of test time to train the model. ECMs describe the cell behavior through an equivalent circuit based on an analogy to electric circuits.

The most commonly used model methodology to describe the electrical battery behavior of thermal management design processes are ECMs [11]. The benefits are an accurate description of the electrical behavior of LIBs with reasonable computational effort, while providing a prediction for the heat generation out of the electrical behavior through the energy balance (Bernardi equation [12]).

Several studies described the influence of the chosen ECM architecture type for the voltage prediction. Wilfeuer et al. [13] studied the parameter dependencies of SOC, temperature, current and pulse test duration on the cell and module levels, by comparing the resulting inner cell resistances. However, they used a simple Rint Model for studying the influence of the parameters on the resistance R_0 while ignoring possible influences on the Open Circuit Voltage (OCV) and heat generation $\dot{Q}$. They have concluded, that the SOC, temperature and pulse test duration need to be considered, while the current dependency should only be included for extreme conditions, e.g., low temperatures.

Regarding LIB thermal management analysis, the chosen ECM architecture and parameter dependencies vary significantly. Current researchers only mention the chosen ECM architecture; Dual Polarization [14] (2021), Thevenin [15] (2021) or Rint [16] (2021) do not give a detailed explanation of the used model [17] (2016). Furthermore, the thermal properties (including the heat transfer coefficient to the environment) are fitted, showing that the model's predicted temperature agrees well with the experimentally measured temperature. This results in a pretended accuracy of the thermal model, which cannot be achieved alone by the different electrical models used.

The heat generation of LIBs is a topical issue. However, current research focus on machine learning algorithms [18,19], the spatial distribution of heat generation within the cell [20] or on the heat generation rate at the limits of the operating range of LIBs [21]. All these studies have in common the fact that on the modeling side they mostly rely on ECMs to predict the generated heat by using the (simplified) Bernardi equation.

Consequently, the research question has been raised to which extent the choice of the ECM architecture and the ECM parameter dependencies influence the predicted LIB heat generation. The goal of this paper is to better understand the impact of the chosen ECM on the design process of the thermal management systems of LIBs and hence, being able to choose the ECM with the least computational effort while not losing model accuracy.

For this purpose, the cylindrical LIB cell LG INR21700 M50 is studied, which is comparable to the Panasonic 21700 cell used in the Tesla Model 3 Long Range in terms of power, nominal voltage and capacity [22,23].

2. Methodology

The methodology consists of two parts. First of all, the electric behavior of LIBs has to be described, and secondly, the thermal model has to be identified.

2.1. Electric Equivalent Circuit Models for Lithium-Ion-Batteries

Electric equivalent circuits are used to describe the input/output current and voltage behaviors of LIBs. These current and voltage behaviors can be described by using an analogy to electric equivalent circuits. The ECMs mostly consist of a voltage source, an OCV, resistors, capacitors, hysteresis and sometimes a Warburg impedance. While these parameters do not represent real electrochemical LIB characteristics, they are able to describe the electrical behavior well [8].

ECMs can generally be divided into two groups. There are the time and the frequency domain ECMs [11]. The difference between the two domains mainly lies in the conducted experiments to parameterize the ECM. While the time domain models focus on a simple current, voltage and temperature measurement apparatus, the frequency domain models require a more complex test system called Electrical Impedance Spectroscopy (EIS). The EIS methodology uses different frequencies to excite the battery and measure the resulting voltage and current response. These results yield a wide range of LIB battery operating points to parameterize the ECM. However, because of the available laboratory environment, this study uses the time domain approach.

2.1.1. The Rint Model

The simplest ECM architecture is called the Rint model, marked as (a) in Figure 1. It consists of an ideal voltage source, called the OCV U_{OCV}, and the internal resistance R_0. By using the equation

$$U_{\mathrm{t}} = U_{\mathrm{OCV}} - I\,R_0 \qquad (1)$$

the terminal voltage U_{t} can be calculated. However, the Rint model has its disadvantages in describing the dynamic behavior of the LIB.

2.1.2. The Thevenin Model

The Thevenin model, shown in Figure 1b, is an improved version of the Rint model. It connects a parallel Resistance-Capacitance (RC) network in series to the existing model parameters to describe the dynamic behavior of the LIB. The RC network consists of a polarization resistance R_1 and an equivalent capacitance C_1 that describe the diffusion voltage drop [8].

The terminal voltage can be determined by

$$U_{\mathrm{t}} = U_{\mathrm{OCV}} - U_1 - I\,R_0 \qquad (2)$$

whereas,

$$\dot{U}_1 = -\frac{U_1}{R_1\,C_1} + \frac{I}{C_1} \qquad (3)$$

is defined as the change in polarization voltage $\dot{U}_1$.

2.1.3. The Dual Polarization Model

The Dual Polarization model (DP) adds a second RC network to the Thevenin model, as shown in Figure 1c. This enables the description of the polarization characteristics more precisely. In the DP model, the polarization is divided into the electrochemical polarization with the first RC network and the concentration polarization with the second RC network. This leads to more accurate model performances [24].

The DP terminal voltage is calculated by

$$U_{\mathrm{t}} = U_{\mathrm{OCV}} - U_1 - U_2 - I\,R_0 \qquad (4)$$

hereby

$$\dot{U}_1 = -\frac{U_1}{R_1\,C_1} + \frac{I}{C_1} \tag{5}$$

defines the change in electrochemical polarization and

$$\dot{U}_2 = -\frac{U_2}{R_2\,C_2} + \frac{I}{C_2} \tag{6}$$

the change in concentration polarization.

In general, the accuracy of ECMs can be improved by using more RC networks in series. However, according to Hu et al. [25], the increased accuracy of more than two RC networks does not overcome the increased computational effort. Since this study tries to find the most accurate ECM for thermal modeling with the least computational effort, two RC networks are the maximum considered.
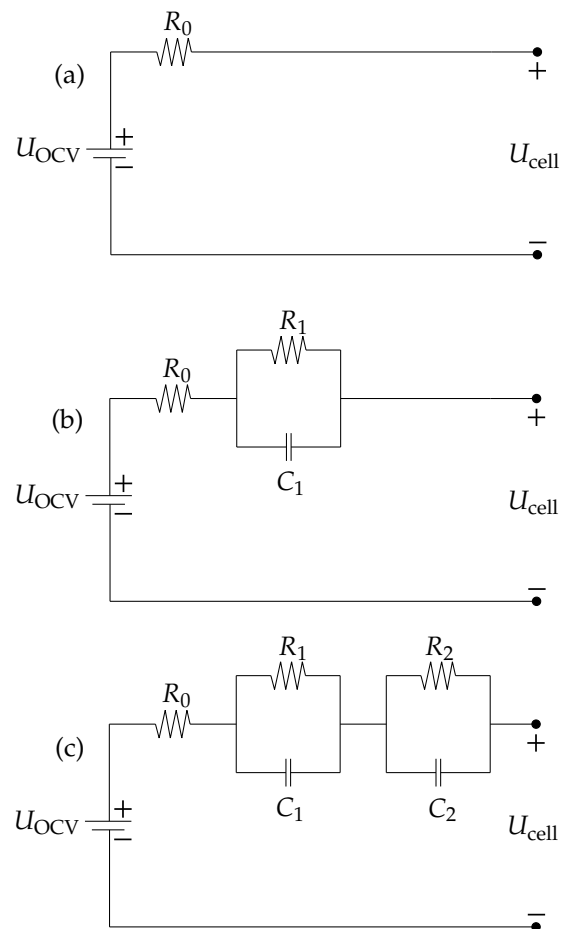

Figure 1. Schematic of (**a**) Rint, (**b**) Thevenin and (**c**) Dual Polarization Equivalent Circuit Model.

2.1.4. Dependencies

First, independent of the usage of ECMs, there is the faradic (coulombic) efficiency. This efficiency describes the generated losses while charging a battery. The coulombic efficiency is defined as

$$\eta_C = \frac{Q_{discharge}}{Q_{Charge}} \tag{7}$$

whereas Q represents the total charge/discharge load. The coulombic efficiency should always be $\eta_C < 1$ [8]. For LIB it is mostly > 0.99 and, therefore, is often neglected and used as $\eta_C = 1$.

The ECM parameter dependencies can be divided into two groups: the OCV and resistance/capacitance dependencies. The OCV can be a function of the SOC, temperature T and hysteresis *hyst*. The resistances/capacitances can be a function of the SOC, temperature T, charge/discharge pulse *cdc* and current I. Furthermore, both groups can be a function of the SOH. Aging phenomena should play no role in the initial decision of the most suitable ECM model for thermal management simulations. Consequently, LIB aging is not considered in this research.

Furthermore, in this study the C-rate is used. The C-rate can be calculated by dividing the applied current I through the nominal capacity C_N. It is defined as $I = 1\,C$ when the current applied fully charges/discharges the LIB in one hour. When the applied current takes two hours to fully charge/discharge the LIB, the C-rate is equal to $I = 0.5\,C$.

2.1.5. State of Charge Estimation

The estimation of the SOC is an essential part of LIB modeling. There are several estimation methods available, while Coulomb Counting and an estimation over the SOC–OCV relationship are the most commonly used techniques.

The Coulomb Counting method is straight forward, integrating the current I over a period of time $[t_0, t_1]$ by

$$\text{SOC} = \text{SOC}_0 - \frac{1}{C_N} \int_{t_0}^{t_1} I(\tau)\mathrm{d}\tau \tag{8}$$

whereas, SOC_0 describes the SOC at t_0. According to Ng et al. [26], the SOC_0 can be estimated by measuring the OCV and taking the corresponding SOC value when the LIB cell is rested for a minimum of 120 min before.

2.2. Heat Generation Calculation

The total heat generated in an LIB can be described by the Bernardi equation [12] in the energy balance form as

$$\dot{Q} = \dot{Q}_{\text{irr}} + \dot{Q}_{\text{rev}} + \dot{Q}_{\text{reac}} + \dot{Q}_{mix} \tag{9}$$

Here, $\dot{Q}_{\text{irr}}$ describes the Joule heating losses, $\dot{Q}_{\text{rev}}$ describes the electrochemical reaction entropy, $\dot{Q}_{\text{mix}}$ are the mixing enthalpy losses in the electrolyte and $\dot{Q}_{\text{reac}}$ represents the heat generation of the side reactions.

When the LIB is used in normal operating conditions, the side reaction losses $\dot{Q}_{\text{react}}$ ([27]) and the mixing losses in the electrolyte $\dot{Q}_{\text{mix}}$ ([28]) can be neglected. Consequently, the heat generation inside of a LIB can be calculated out of the ECM parameters through the simplified Bernardi equation

$$\dot{Q}_{\text{loss}} = I\,(U_{\text{OCV}} - U_{\text{t}}) - I\,T\,\frac{\partial\,U_{\text{OCV}}}{\partial\,T} \tag{10}$$

where, U_{t} is the cell terminal voltage and $\partial U_{\text{OCV}}/\partial T$ is the LIB entropic coefficient [12]. This is because current sign convection charging the cell is defined as a negative current and discharging is equal to a positive current in this study.

2.3. Thermal Model

Computational Fluid Dynamics software Star CCM+ has been used for all studies conducted in this paper. The ECM has been included by using the Battery Equivalent Circuit Model tool by Star CCM+. A simple cylinder geometry with the battery cell dimensions is

used. For solving the thermal model, Star CCM+ uses a finite volume method where the integral form of the energy balance

$$\frac{\partial}{\partial t} \int_V \rho\, E\, \mathrm{d}V + \oint_A \rho\, H\, v\, \cdot\, \mathrm{d}a = -\oint_A \dot{q}''\, \cdot\, \mathrm{d}a +$$
$$\oint_A T\, \cdot\, v\, \mathrm{d}a + \int_V f_\mathrm{b}\, \cdot\, v\, \mathrm{d}V + \oint_A \sum_i h_i\, J_i\, \mathrm{d}a \tag{11}$$

is solved, which is described in more detail in the Simcenter User Guide [29]. The heat generation in Star CCM+ is calculated, as shown in Equation (10), neglecting phase change and mixing losses [29]. For the purpose of this paper, which is to study the influence of ECM parameters and architectures on the predicted voltage and heat generation, the thermal model has a secondary importance. Hence, the established assumptions and boundary conditions for the thermal model are only briefly discussed.

2.3.1. Assumptions

Heat generation has been assumed as uniform throughout the whole battery cell, as previously carried out by many researchers [14–16,30]. Furthermore, it has been necessary to set two different types of boundary conditions. First, the coat of the battery cell is taken as adiabatic because the coat has been wrapped around with thermal insulation tape to minimize the environmental influence on the temperature development in the experimental validation runs. Since there are electrical contacts on both collector sides, they could not be isolated. This results in the second boundary condition for both collector sides, which takes the summed up effect of heat convection and heat radiation into account. The simulation time step is set to $\Delta t = 1\,\mathrm{s}$ because of the chosen highly dynamic WLTC cycle for the model validation. Two inner iterations per time step have been used to adequately solve the electrical and thermal model. For every time step, the resulting volume averaged battery cell temperature is used as the input temperature for the ECM.

2.3.2. Heat Convection and Heat Radiation

Heat convection is defined as

$$\dot{Q}_\mathrm{conv} = h_\mathrm{conv}\, A\, (\Delta\, T) \tag{12}$$

where, h_conv represents the heat transfer coefficient, A the involved surface in the heat transfer and ΔT the temperature difference between the surface and ambient temperatures. For free convection on a cylinder, the Nusselt number Nu can be calculated according to Klan [31] by the Nusselt correlation

$$Nu = \left\{0.752 + 0.387\, \left[Ra\, f_3(Pr)\right]^{1/6}\right\}^2 \tag{13}$$

while the Nusselt number Nu and Rayleigh number Ra are calculated with the length $L = \frac{\pi}{2}\, d$. The function $f_3(Pr)$ is defined as

$$f_3(Pr) = \left[1 + \left(\frac{0.559}{Pr}\right)^{9/16}\right]^{-16/9} \tag{14}$$

depending only on the Prandtl number Pr.

Heat radiation can be calculated according to Stephan [32] by

$$\dot{Q}_\mathrm{rad} = \epsilon\, \sigma\, A\, (T_2^4 - T_1^4) \tag{15}$$

whereas, ϵ represents the emissivity of the surface material, σ is the Stefan–Boltzmann constant, A is the surface involved in the heat radiation and $T_{1,2}$ is the temperatures on the ambient and surface.

3. Experimental Setup and Parameter Identification

In this section, firstly the experimental setup and examined test procedures are presented. Secondly, the used parameter identification methodology is introduced.

3.1. Battery Test Bench

To conduct the necessary tests, a battery test bench was used. The battery test bench is composed of a Basytec HPS battery tester system with one channel, a computer on which the Basytec Software is installed and a climate chamber from Weiss Umwelttechnik GmbH. Furthermore, a cylindrical cell holder with integrated voltage and temperature measurement from the company FEINMETALL was used to measure the cell voltage. The experimental platform is shown in Appendix A Figure A1.

The voltage range of the battery tester is 0–6 V and the current range is ±60 A. The maximum error in the voltage detection is at 1 mV and 0.05% Full Scale in the current detection [33]. The workflow for the development of a LIB ECM is well documented in the literature, as, e.g., by Nikolian et al. [34]. It consists of a characterization, parameter identification and validation process. The electrical characterization process can be divided into three different types: capacity test, OCV-SOC-test and High Pulse Power Characterization (HPPC). Furthermore, to capture the reversible heat generation term, an entropic coefficient test is necessary. The individual test procedures are described in the following.

3.1.1. Capacity Test

The capacity test comprises a full charge of the cell and a full discharge afterwards according to the manufacturer's recommendation. Through the Ampere-Hour integration

$$C_N = \int_{t_0}^{t_{end}} I(\tau) d\tau \tag{16}$$

the nominal capacity C_N of the LIB can be calculated.

According to Belt [35], the procedure should be repeated until the difference in discharge capacity is less than 2% for three consecutive complete discharge cycles. Furthermore, the capacity of a LIB is dependent on the cell temperature T_{cell}. Hence, the capacity test needs to be examined at different test temperatures $C_N = f(T)$.

3.1.2. OCV-SOC Test

For determining the OCV-SOC curve, there are two different approaches. Firstly, the constant current method (CCM), and secondly, the relaxation method (RM) [36].

The CCM is to perform low constant current charge or discharge processes over the whole LIB SOC range. According to Plett [8], a current of $C_N/30$ is sufficient to depict a current where neglectable losses and heat generation occur in the LIB. Therefore, the resulting measured voltage over the SOC range of the battery can be taken as the actual OCV.

The RM is to discharge the LIB in sufficient (e.g., 5, 10%) SOC steps while resting the LIB for an adequate time t_{rel} after each step for the relaxation process. It is assumed that the voltage measured after the relaxation time t_{rel} represents the OCV at the SOC. The procedure needs to be examined for discharge and charge to get the hysteresis behavior of the LIB.

3.1.3. HPPC Test

The last test procedure is the HPPC. It has been defined by Belt [35] to capture the dynamic behavior of a LIB with an ECM. Consistent to the capacity test, the HPPC test procedure needs to be performed for different cell temperatures T_{cell} as well. Additionally, varying charging/discharging current pulses should be used. The more data points are available to parameterize the ECM, the more accurate the ECM will be to describe the dynamic behavior of the LIB. However, those tests can take up to one week for one test temperature T_{test}. Hence, a good trade-off between accuracy and test time is desirable.

3.1.4. Entropic Coefficient Test

There exist two methods to determine the entropic coefficient. The first option is to use the results of the OCV determination at different test temperatures (OCV method). The second option, which requires an additional test procedure, is the state-of-the-art method for the determination of the entropic coefficient (EC method).

The OCV method utilizes the results of the SOC-OCV tests at different temperatures for the determination of the entropic coefficient [37]. For each SOC point, the gradient of the OCV over the temperature can be calculated, resulting in the entropic coefficient. Geifes et al. [37] have shown the linear behavior of the entropic coefficient over varying temperatures. Therefore, it is already sufficient to use the OCV results of only two different temperature data points.

The EC method as, for example, proposed by Forgez et al. [38], can be divided into several steps. The battery cell is soaked at the test temperature $T_{\text{test,1}}$, resulting in an OCV $U_{\text{OCV,1}}$. Afterwards, the test temperature is set to $T_{\text{test,2}}$ and the cell is soaked again. The resulting OCV $U_{\text{OCV,2}}$ enables the calculation of the entropic coefficient term by

$$\frac{\partial U_{\text{OCV}}}{\partial T}(\text{SOC}) = \frac{U_{\text{OCV,2}}(\text{SOC}) - U_{\text{OCV,1}}(\text{SOC})}{T_{\text{test,2}} - T_{\text{test,1}}} \tag{17}$$

depending just on the SOC. While the usage of the OCV method saves additional test time, the EC method is more reliable and accurate since it is not dependent on the defined relaxation time of the OCV test.

3.2. ECM Parameter Identification

With the chosen test procedure, the ECM parameters can be identified. Depending on the desired level of detail, different ECMs can be generated. Representing the parameter identification process, the process is explained for a DP model. The parameter identification process is an advanced version of the method proposed by Zhu et al. [39].

In case of the DP model, there are six parameters to be identified: the OCV U_{OCV}, the ohmic resistance R_0, the electrochemical polarization resistance R_1, the electrochemical transient capacitance C_1, the concentration polarization R_2 and the concentration transient capacitance C_2. The OCV can be determined separately from the other five parameters.

3.2.1. Open Circuit Voltage

The OCV is identified using the RM or CCM test results. Regarding the RM, the OCV is taken as the measured voltage after the relaxation time t_{rel} for every 5% SOC step. Furthermore, the OCV is determined for the SOC steps while charging and while discharging. This enables the possibility to distinguish between charge and discharge OCV in the ECM (hysteresis). When using the CCM method, the measured voltage equals the OCV over the full SOC range. The SOC-OCV results are stored in Look-Up-Tables (LUT).

3.2.2. Resistances and Capacitances

The resistances and capacitances parameter identification process represents an advanced method of the process proposed by Zhu et al. [24]. In the following, the process is explained in detail for one exemplary pulse test result shown in Figure 2. Here, t_{a} is the start time of the pulse, t_{c} is the end time of the pulse and t_{e} is the end time of the relaxation process.

The terminal voltage of a DP model is calculated, as shown in Equation (4). To describe the dynamic LIB behavior, the polarization voltages have to be time dependent and are defined as

$$U_i(t) = U_{\text{RC},i} \exp\left(-\frac{t - t_{\text{c}}}{\tau_i}\right) \tag{18}$$

whereas, $U_{RC,i}$ represents a calculation variable and τ_i is equal to $\tau_i = R_i C_i$. This results in

$$U_t(t) = U_{OCV} - U_{RC,1} \exp(-\frac{t - t_c}{\tau_i})$$
$$-U_{RC,2} \exp(-\frac{t - t_c}{\tau_i}) - I R_0 \tag{19}$$

for the calculation of the terminal voltage U_t. Since the OCV is already determined in the first parameter identification step, it can be subtracted here, normalizing all measured pulse end voltages to $U(t_e) = 0$. This leads to the parameter identification equation

$$U_{model}(t) = -U_{RC,1} \exp(-\frac{t - t_c}{\tau_i})$$
$$-U_{RC,2} \exp(-\frac{t - t_c}{\tau_i}) - I R_0 \tag{20}$$

whereas, U_{model} stands for the predicted voltage by the ECM. This equation is used to optimize the parameters $U_{RC,i}$, τ_i and R_0 by the Matlab gradient optimization function *lsqnonlin* on the measured voltage results for time span t_c to t_e. Using the optimized parameters, the polarization resistances R_i

$$R_i = \frac{U_{RC,i}}{I \left(1 - \exp(-\frac{t_c - t_a}{\tau_i})\right)} \tag{21}$$

can be calculated for $i = 1, 2$. The resulting optimized five dynamic ECM parameters R_i, τ_i are added to the SOC-OCV LUTs. As such, the parameter identification process is finalized.
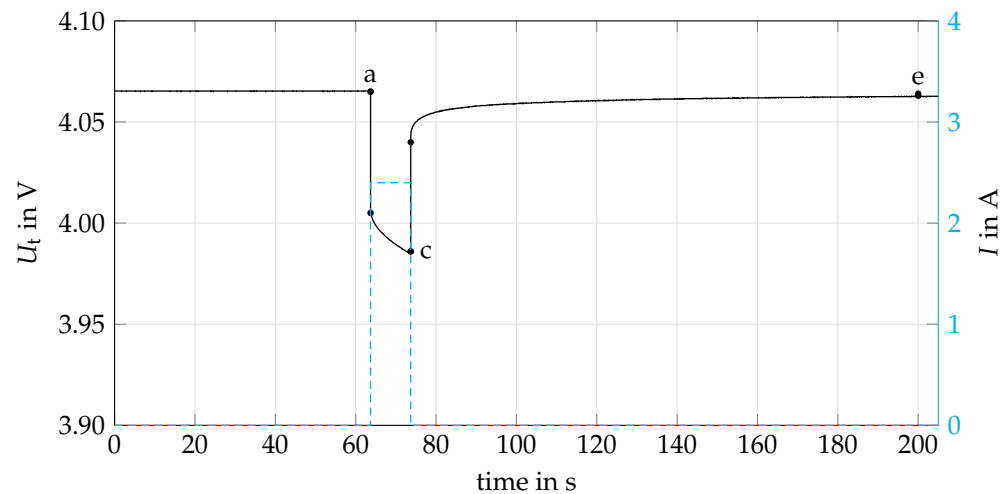

Figure 2. Measured 0.5 C-Rate current pulse and voltage behavior to identify the parameters for the different ECMs.

In this study, a Matlab parameter identification tool has been developed using the described process. This tool enables the user to optimize the ECM parameters on chosen dependencies and ECM architectures. By providing the Matlab tool with the conducted HPPC test results as an input, the user can choose between considering the parameter dependencies of OCV hysteresis *hyst*, OCV temperature T, resistance/capacitance temperature T, resistance/capacitance charge/discharge pulse *cdc* and resistance/capacitance current I. In Table 1, the parameter identification assumptions for considering or neglecting these dependencies are shown. Furthermore, all dependency studies can be conducted for a DP, Thevenin and Rint ECM architecture.

Table 1. Explanation of the ECM parameter dependencies when including them (dependent) or neglecting them (independent) in the developed Matlab tool.

	Dependent	**Independent**
I	LUTs for every tested current pulse value	LUT for optimized value of all tested current pulses
cdc	LUTs separately for charge and discharge pulses	LUT for optimized value of both charge and discharge pulses
$hyst$	LUTs for charge OCV and discharge OCV	LUT taking the arithmetic middle between charge and discharge OCV
T	LUTs for all conducted test temperatures	LUT only for $T_{\text{test}} = 25\,^\circ\text{C}$

4. Results and Discussion

In the following, the experimental test results, the validation profile and the comparison of the voltage and heat generation results of the studied ECMs are shown.

4.1. Experimental Results

The experimental results present the capacity, OCV-SOC, HPPC and entropic coefficient results.

4.1.1. Capacity Test Results

Before any battery test procedure is examined, the studied LIB is activated by five full charge/discharge cycles according to the manufacturer's data sheet [23]. The capacity test procedure is performed as explained in Section 3.1.1. For this study, three different temperatures $T_{\text{test}} = 5, 25, 45\,^\circ\text{C}$ were selected. The analyzed temperature range is limited at the bottom side to $T_{\text{test}} = 5\,^\circ\text{C}$. If the temperature is $T < 5\,^\circ\text{C}$, the battery pack in the BEVs would be preconditioned to avoid degradation of the battery cells. Too high operating temperatures $T > 45\,^\circ\text{C}$ also result in a degradation of the battery cell or can even lead to thermal runaway events, so the upper limit is set to $T_{\text{test}} = 45\,^\circ\text{C}$. The resulting discharge nominal capacities C_{N} are shown in Table 2.

Table 2. Capacity test results for the studied cell at the selected test temperatures.

	Nominal Capacity C_{N} in mA h		
T_{test}	5 °C	25 °C	45 °C
LG 21700	4590	4800	4720

4.1.2. OCV-SOC Test Results

The OCV-SOC relationship results are determined by both test procedures, the CCM and the RM test procedure. For the RM test procedure, a pre-test was examined. At all three test temperatures T_{test}, the necessary relaxation time t_{rel} for the determination of the OCV was studied at SOC = 50%. The results show that at the test temperature of $T_{\text{test}} = 25\,^\circ\text{C}$, the requirement was fulfilled after $t_{\text{rel}} = 40\,\text{min}$. However, the required relaxation time increases at low SOCs and low test temperatures T_{test}. Therefore, a safety margin was used. The relaxation time was increased to $t_{\text{rel}} = 2\,\text{h}$ for the OCV determination to ensure thermal and chemical equilibrium at all test temperatures and SOCs while still maintaining a reasonable total test time. Furthermore, SOC steps of 5% were taken to accurately determine the OCV–SOC relationship.

Figure 3 shows the OCV–SOC relationship for the CCM $I = C_{\text{N}}/30$ and the RM test procedure at test temperature $T_{\text{test}} = 25\,^\circ\text{C}$. As can be seen, the CCM test results show a stronger hysteresis relationship compared to the RM. According to Plett [8], the CCM test procedure assumes that the battery cell is close to electrochemical and thermal equilibrium if the current is small enough. However, the CCM equals a stronger hysteresis compared to the RM because of the non-linear behavior of the LIB polarization processes [36]. Consequently, the RM results are used in this study. This enables the proposed test procedure to be simplified, as can be seen in Figure A2 in the Appendix A. The simplified test procedure combines the OCV-SOC test and the HPPC test. For this purpose, after every 5% SOC step

is set, a relaxation time of $t_{rel} = 2\,h$ is taken to measure the OCV at the respective SOC. After the relaxation time t_{rel}, the HPPC profile is run and the procedure is repeated for every SOC step both for charging and discharging.
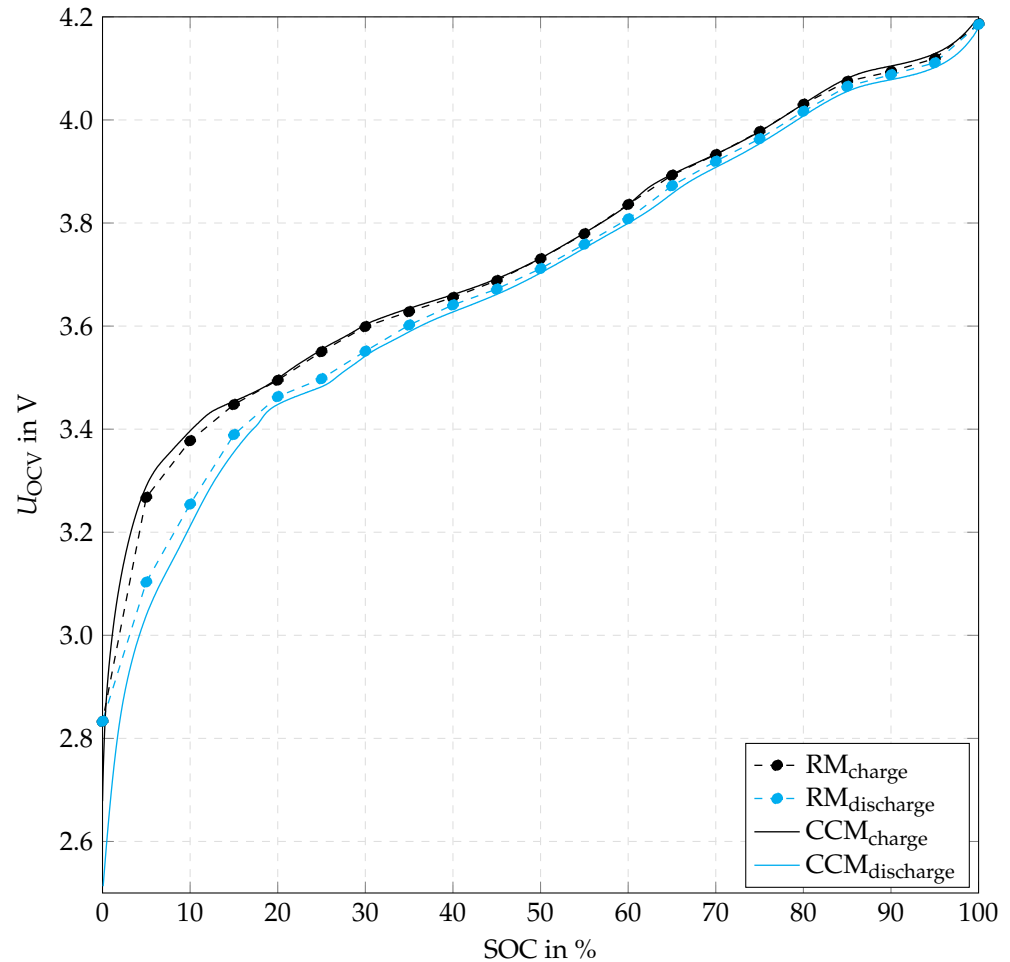

Figure 3. Comparison of Constant Current Test Method (CCM) and Relaxation Test Method (RM) results for the determination of the OCV–SOC relationship at test temperature $T_{test} = 25\,°C$.

4.1.3. HPPC Test Results

The HPPC test was examined, as proposed by Belt [35], with two adjustments employed to achieve better ECM accuracy. Firstly, the rest time after every current pulse was increased from $t_{rest,pulse} = 40\,s$ to $t_{rest,pulse} = 600\,s$ to better capture the dynamic LIB response to the pulse. Furthermore, the recharge pulse was set at the same current as the discharge pulse to not change the SOC of the battery over a HPPC profile. Another benefit of this adjustment is being able to distinguish between charge and discharge pulse responses. The current pulse time was kept at $t_{pulse} = 10\,s$.

The HPPC profile was run at every 5% SOC steps for charging and discharging. The current pulses tested are $I = 0.2, 0.5, 1, 2\,C$. However, the maximum possible current pulses vary with different SOC levels and are adapted to the manufacturer's data sheet [23]. The HPPC procedure is performed at all three test temperatures mentioned in Section 4.1.1. The measured voltage results are used to identify the ECM parameters, as explained in Section 3.2. The test time necessary for a HPPC profile at $T_{test} = 25\,°C$, including OCV-SOC determination, is equal to $t_{HPPC} = 4.5 \times 10^5\,s = 125\,h$ excluding the previous constant-current-constant-voltage-charge and soaking time.

4.1.4. Entropic Coefficient Test Results

Both methods proposed in Section 3.1.4 are studied. First, the results for the OCV method are discussed. The OCV-SOC measurements at different test temperatures $T_{\text{test}} = 5, 25, 45\,°C$ were used to evaluate the OCV change $\partial U_{\text{OCV}}/\partial T$ over the temperature. However, the results show that at high and low SOCs the relaxation time t_{rel} for $T_{\text{test}} = 5\,°C$ is not sufficient to achieve thermal and chemical equilibrium inside the LIB. Hence, the assumption by Geifes et al. [37] of the linear behavior of the entropic coefficient with the temperature change is taken. This enables the possibility to only use the OCV results of $T_{\text{test}} = 25\,°C$ and $T_{\text{test}} = 45\,°C$ to determine the entropic coefficient. The OCV method results are shown in Figure 4.
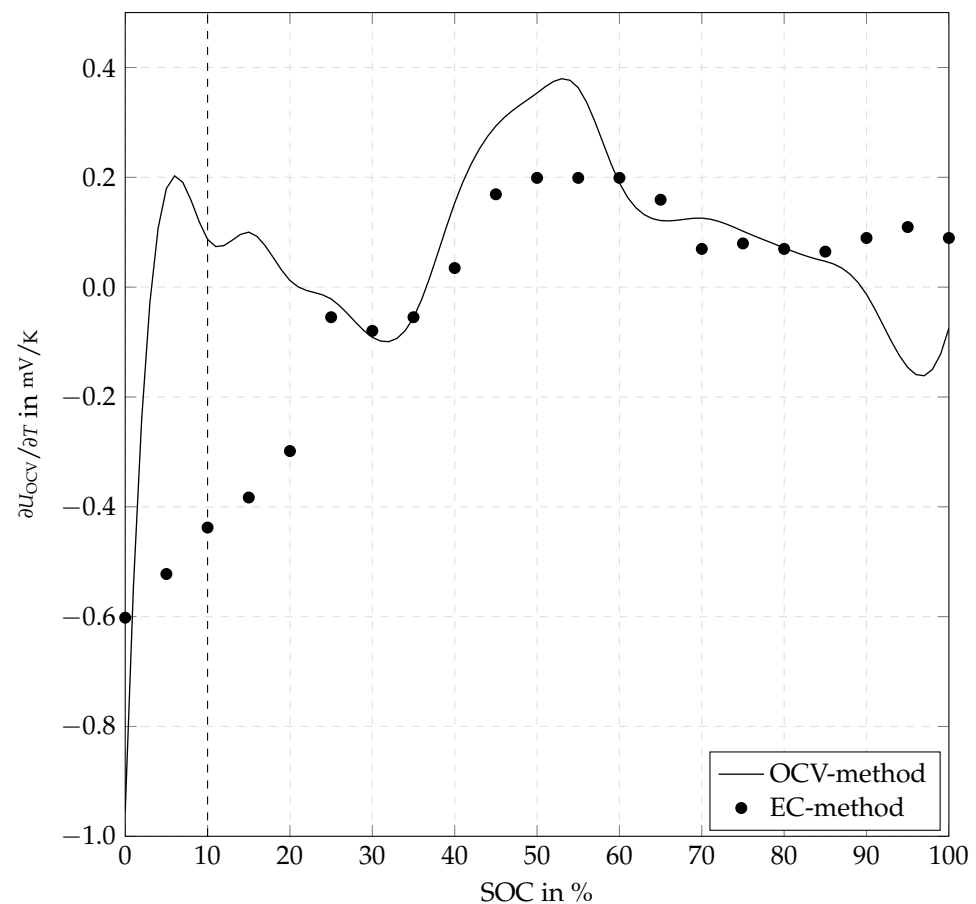

Figure 4. Entropic coefficient results using the Open Circuit Voltage (OCV) method and the Entropic Coefficient Test (EC) method by comparison.

The EC method could be examined as explained in Section 3.1.4. The rest time after every temperature change was set to $t_{\text{rest}} = 4$ h. Consistently to the OCV-SOC and HPPC test, 5% SOC steps and the three test temperatures T_{test} were taken for the determination. The results are shown in Figure 4. The OCV method and the EC method show no good agreement. Especially in low and high SOC regions, the results between the two methods have large deviations. The reason, therefore, can be identified by analyzing the gradient of the OCV over time $\partial U_{\text{OCV}}/\partial t$ in the last ten minutes before the OCV measurement points for both analyzed methods. Adequate results expect the gradient at the OCV measurement point to be equal to zero $\partial U_{\text{OCV}}/\partial t = 0\,\text{V/h}$.

For the OCV method, $\partial U_{\text{OCV}}/\partial t$ is not equal to zero, especially in the high and low SOC regions, where the differences for the two methods can be identified the most. Hence, the thermal and chemical equilibrium have not been achieved. Looking at $\partial U_{\text{OCV}}/\partial t$ of the EC method, the gradients are zero, except for the really low SOC region SOC < 5%. The reason

for the difference can be identified in the chosen rest time $t_{\text{rel}}(\text{EC method}) = 2\,t_{\text{rel}}(\text{OCV method})$. Furthermore, the EC results agree well with the results of Geng et al. [40]. Hence, for all simulations the EC method results are used as entropic coefficient LUTs. All examined test procedures are summarized in Appendix A Figure A2.

4.2. Thermal Modeling Results

In the following, the calculated and assumed thermal parameters of the investigated LIB cell are presented. The thermal parameters are the LIB density, specific heat capacity and anisotropic heat conductivities. For the determination of the density, the LIB has been weighed and the volume has been calculated out of the LIB dimensions. This results in the LIB density of $\rho = m_{\text{cell}}/V_{\text{cell}} = 2792.7\,\text{kg/m}^3$.

The specific heat capacity and the thermal conductivities are taken from Steinhardt et al. [41] and Bui et al. [42] as $c_{\text{p}} = 850\,\text{J/kg\,K}$, $k_{\text{r}} = 1.4\,\text{W/m\,K}$ and $k_{\phi,\text{z}} = 30\,\text{W/m\,K}$. The thermal conductivity in tangential direction $k_{\phi} = k_{\text{z}}$ is assumed to be the same as in the axial direction.

Lastly, for the heat convection and radiation boundary condition, the heat transfer equations for convection (Equation (12)) and radiation (Equation (15)) were solved on the heat transfer coefficient. By adding up both heat transfer coefficient equations, a boundary condition could be set in Star CCM+ for both collector surfaces, which considers the corresponding surface averaged temperature $T_{\text{avg}}(z)$ and the measured ambient temperature T_{amb} for the calculation of the transferred heat. The emissivity is assumed to be $\epsilon = 0.3$. The boundary condition at the coat surface is adiabatic. Furthermore, a mesh independence study was successfully completed, showing no influence of the chosen mesh base size on the simulation results. Figure 5 shows the mesh and boundary conditions of the thermal model used in this study.
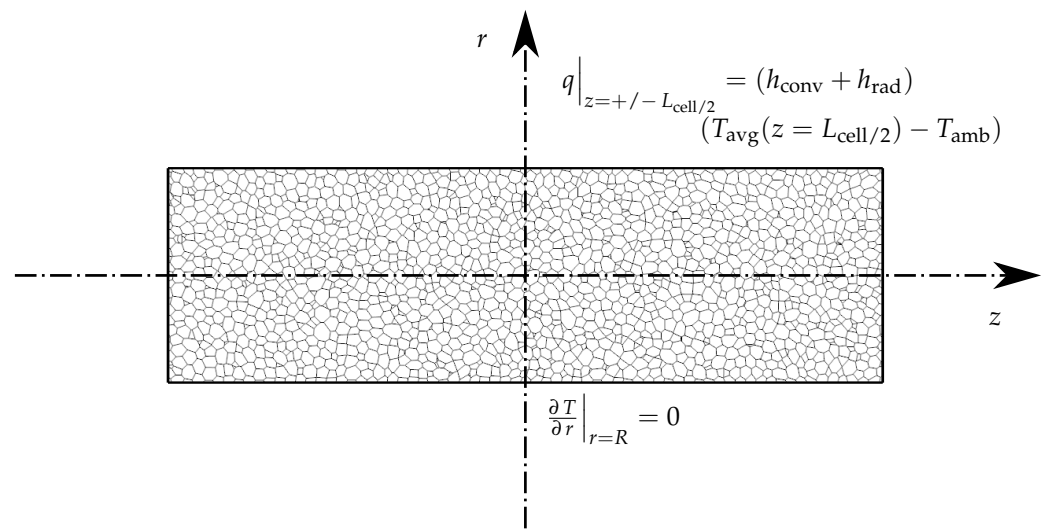

Figure 5. Cut through the rz-plane of the used thermal model and boundary conditions in Star-CCM+ for the multi-physics simulation.

4.3. Validation Profile

First, the current-time WLTC profile for the studied LIB corresponding to the velocity-time WLTC profile has to be evaluated. This is derived from several assumptions taken by the comparison with a Tesla Model 3 Long Range [43]. The resulting cycle is shown in Figure 6, whereas the current is normalized with the nominal capacity C_{N} (C-rate). This profile is used in the experimental setup as well as in the numerical simulation.

For the validation of the models, the WLTC profile was examined at three SOC-steps (25, 50, 75%) and three temperatures ($T_{\text{amb}} = 15, 25, 35\,°C$). The SOC steps were chosen to cover the usable battery range for the application in BEVs and the temperatures have been chosen to enable evaluation of the temperature dependency of the ECMs. In

total, the studied LIB cell was cycled 23 times to obtain the electrical model before the validation profiles was examined. This corresponds with a SOH > 99% according to the manufacturer's data sheet [23].
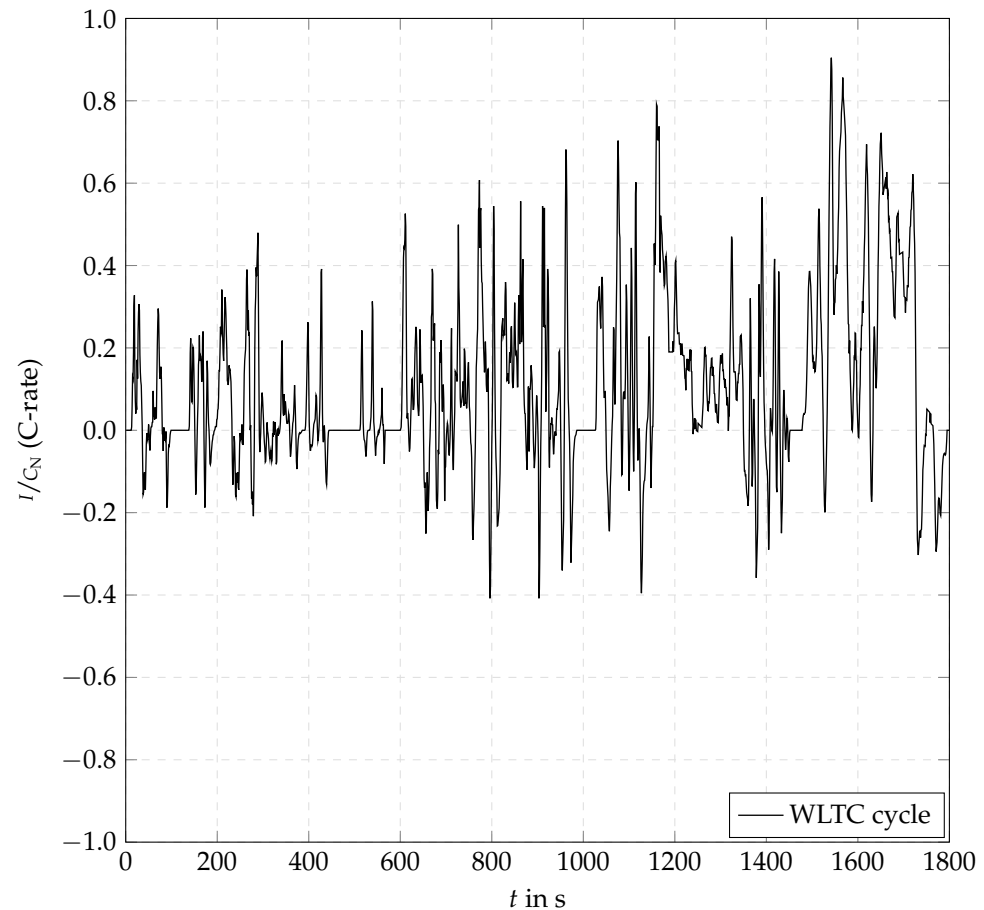

Figure 6. World Harmonized Light Vehicle Test Cycle (WLTC) for the validation of the studied ECMs.

4.4. Voltage Validation and Comparison ECMs

In total, there were eight different ECMs studied, labeled ECM_{1-8}. They are shown in Table 3 and can be divided into three groups. First, the ECM parameter dependency group ECM_{1-5}, second, the test parameters ECM_6 and third, the ECM architectures $ECM_{7,8}$.

Table 3. Studied ECMs with different parameter dependencies, test parameters and ECM architectures.

	Open Circuit Voltage U_{OCV}	Ohmic Resistance R_0	Resistance/Capacitance R_1/C_1	Resistance/Capacitance R_2/C_2	SOC Data Points
ECM_1	f(SOC,*T*,*hyst*)	f(SOC,*T*,cdc,*I*)	f(SOC,*T*,cdc,*I*)	f(SOC,*T*,cdc,*I*)	5% steps
ECM_2	f(SOC,*T*,*hyst*)	f(SOC,*T*,cdc)	f(SOC,*T*,cdc)	f(SOC,*T*,cdc)	5% steps
ECM_3	f(SOC,*T*,*hyst*)	f(SOC,*T*,*I*)	f(SOC,*T*,*I*)	f(SOC,*T*,*I*)	5% steps
ECM_4	f(SOC,*hyst*)	f(SOC,cdc,*I*)	f(SOC,cdc,*I*)	f(SOC,cdc,*I*)	5% steps
ECM_5	f(SOC,*T*)	f(SOC,*T*,cdc,*I*)	f(SOC,*T*,cdc,*I*)	f(SOC,*T*,cdc,*I*)	5% steps
ECM_6	f(SOC,*T*,*hyst*)	f(SOC,*T*,cdc,*I*)	f(SOC,*T*,cdc,*I*)	f(SOC,*T*,cdc,*I*)	10% steps
ECM_7	f(SOC,*T*,*hyst*)	f(SOC,*T*,cdc,*I*)	f(SOC,*T*,cdc,*I*)	-	5% steps
ECM_8	f(SOC,*T*,*hyst*)	f(SOC,*T*,cdc,*I*)	-	-	5% steps

For the ECM parameter dependency group, the influence of the current, charge/discharge pulses, temperature and hysteresis are studied. Regarding the test parameters, ECMs were

parameterized with the test results for every 5% SOC steps and 10% SOC steps. Hindermost, the influence of choosing a Rint, Thevenin and DP model is studied.

The absolute error for the comparison of the ECMs is calculated by

$$err_{\text{U}}(t) = \frac{U_{\text{exp}}(t) - U_{\text{ECM}}(t)}{U_{\text{exp}}(t)} \tag{22}$$

for every temporal point t. This means that a negative error is an ECM overprediction of the voltage; thus, a positive error is an ECM underprediction of the voltage. The mean WLTC voltage error is calculated by

$$err_{\text{U,mean}} = \frac{\sum_{t=0}^{t_{\text{end}}} |err_{\text{U}}(t)|}{t_{\text{end}}} \tag{23}$$

and used for the comparison of the accuracy of the ECM models.

The results of the experiment and the ECM_1 simulation voltage, as well as the error err_{U} for a WLTC at $T_{\text{amb}} = 25\,°C$ and SOC $= 25, 50, 75\,\%$ are shown in Figure 7. It can be seen that the simulation underpredicts the LIB resistance for all three SOC starting points resulting in an overprediction of the LIB terminal voltage U_{t}. Hence, there is an increasing negative error err_{U}. The error can be caused due to not using enough RC networks for the modeling of the dynamic LIB behavior. Furthermore, the validation tests were examined after the characterization cycles. This could lead to LIB aging, which has already increased the battery resistance. However, the mean errors at all three SOCs are still small $|err_{\text{U,mean}}| = 0.254\% - 0.366\,\%$.
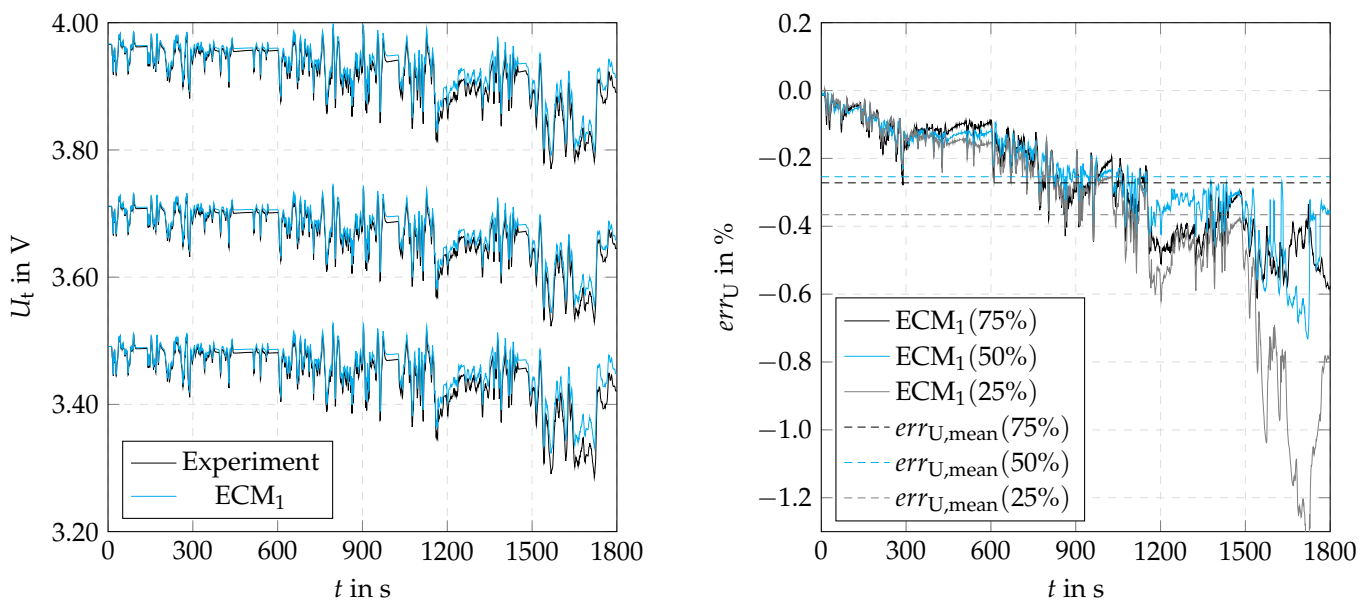

Figure 7. Left: Experimental and ECM_1 voltage results; **Right**: ECM_1 error compared to the experimental results for a WLTC profile at SOC $= 25, 50, 75\%$ and $T_{\text{amb}} = 25\,°C$.

4.4.1. Assumptions

To enable a comparison between the ECMs, several assumptions have to be made. To get an adequate comparability, SOC correction on the measured OCV is assumed to be performed at the beginning of the WLTC $t = 0$. Referring to Section 2.1.5, this assumption is valid since a rest time of $t_{\text{rest}} > 120\,\text{min}$ is fulfilled before every WLTC cycle. Hence, the SOC for every model is adapted so the start OCV $U_{\text{OCV}}(t = 0)$ is the same for every compared ECM. This results in an error of the test profile of $err_{\text{U}}(t = 0) = 0\,\%$ for all studied ECMs. The start SOC values used in the simulation for all ECMs can be seen in Appendix A Table A1.

The ECM parameter dependency studies were examined with a DP model. In total, nine simulations (three SOC starting points SOC = 75, 50, 25% at three different ambient temperatures T_{amb} = 15, 25, 35 °C) were experimentally tested and simulated for all studied ECMs. The discussion of the results regarding the voltage prediction is carried out by using Figure 8 (left). Since the changing ambient temperature only has an influence on the temperature dependency study (ECM$_4$), the mean errors are averaged for every SOC starting point over all three temperatures $\sum_{i=1}^{3} err_{U,mean}(T_{amb,i})/3$. Additionally, the mean error over all nine WLTC cycles is shown in Figure 8 (right). The results are mainly discussed in comparison to the ECM$_1$, where all dependencies are considered and a DP model with 5% SOC steps is used.
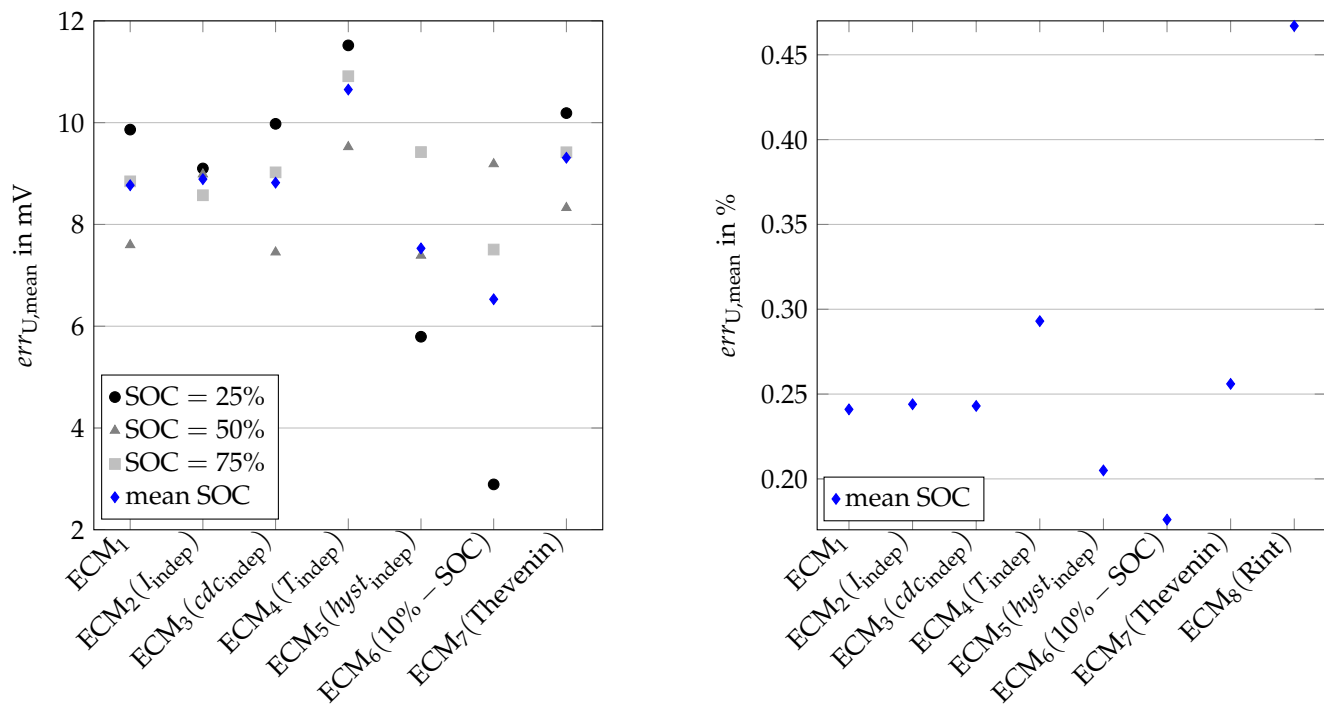

Figure 8. Comparison of studied ECMs: **Left**: absolute voltage error in mV; **right**: voltage error in %. Values at SOC points are averaged over three temperatures.

4.4.2. ECM Parameter Dependencies

First, the accuracy while considering the ECM parameter dependency of the current is analyzed. For this purpose, all other dependencies have been included and just the current dependency is changed. As can be seen in Figure 8(left), the mean SOC voltage error increased by 0.12 mV (1.4%) compared to the ECM$_1$. The discrepancy is in a reasonable range of the measuring accuracy, so the influence of the current dependency on the voltage prediction is neglectable. This can as well be seen in the LUT results for the different currents applied, as the identified resistances have relatively small deviations. Hence, the results agree well with Wildfeuer et al. [13].

The influence of the charge/discharge pulse dependency on the voltage prediction is even less. The mean SOC voltage error increases by 0.05 mV (0.6%) compared to the ECM$_1$. Consequently, the LIB internal resistance is not dependent on the direction of Lithium-Ion transport inside the cell, but more on the absolute value of the current. This corresponds well with the data in the literature, where the charge pulse usually is used as regeneration pulse to the previously examined discharge pulse.

The temperature dependency has a strong influence on the accuracy of the ECM. This can be seen for all three evaluated SOC points, with a mean SOC voltage error increase up to 21.4% compared to the ECM$_1$. If the results for the temperature of T_{amb} = 25 °C were ignored, the mean SOC voltage error increases even more. This is due to the fact that the battery

inner resistance and reaction (Arrhenius equation) changes with the temperature. Hence, the lower the temperature the higher the LIB resistance compared to the recommended operating temperature. This leads to underpredicted resistances at lower temperatures. As can be seen in Figure 7, the ECM of all dependencies underpredicts the LIB resistance. Consequently, using the already too low LIB resistances at $T_{\mathrm{amb}} = 25\,^{\circ}\mathrm{C}$ for the voltage prediction at $T_{\mathrm{amb}} = 15\,^{\circ}\mathrm{C}$, the ECM voltage error further increases. Temperature dependency needs to be considered to achieve better ECM accuracy in the voltage prediction.

The discussion of the hysteresis dependency is strongly related to the SOC correction assumption. The SOC correction is the reason why the model neglecting hysteresis starts at different SOCs than the previously discussed ECMs, as can be seen in Appendix A Table A1. The WLTC cycle starts after a discharge process. Hence, for the ECMs considering hysteresis the measured discharge OCV equals the start OCV for the simulation. When hysteresis is ignored, the OCV at the same SOC point is generally higher. In consequence, for a hysteresis independent ECM with SOC correction, the start SOC will be lower compared to the hysteresis dependent model. Lower SOCs equal higher LIB resistances in the low SOC region SOC < 25%. Since the ECM_1 with all dependencies underpredicts the resistance, ignoring the hysteresis effect leads to a 14% decreased mean SOC voltage error compared to the ECM_1.

4.4.3. ECM Test Parameter

The mean SOC voltage error is 25.5% less with the usage of 10% SOC step data points compared to the 5% SOC step data points used for the ECM_1. Expecting more accurate results with more experimental data points, the opposite can be seen here. Especially for the 25% SOC, the ECM_6 is more accurate. The explanation lies, as for the hysteresis dependency, in the assumed SOC correction. At SOCs lower than 25%, the SOC-OCV gradient starts to increase significantly. For the 10% SOC step model, there are only measured OCVs at 20% and 30% available. As previously explained, the model start SOC is adapted on the start OCV. This results in $T_{\mathrm{amb}} = 25\,^{\circ}\mathrm{C}$ and SOC=25% in a 1.9% lower start SOC $(\mathrm{SOC}(\mathrm{ECM}_1) = 24.1\%, \mathrm{SOC}(\mathrm{ECM}_6) = 22.2\%)$, as can be seen in Appendix A Table A1. At lower SOCs, the LIB resistance is higher, which leads to more accurate voltage predictions in this case. Compared to the hysteresis dependency, the interpolation between SOC data points further increases the taken resistances by the ECM.

4.4.4. ECM Architecture Influence

For the Thevenin (ECM_7) architecture, the voltage error increases by 6.2% compared to the DP model ECM_1. While the tendencies are the same, the missing RC network cannot model the dynamic behavior of the LIB voltage as accurately as the DP model.

The mean SOC voltage error by the Rint model ECM_8 of 17.29 mV is too high to be shown in Figure 8 (left). However, in Figure 8 (right), it can be seen that the error is almost doubled compared to the DP model ECM_1. Hence, the completely missing modeling of the dynamic LIB behavior in the Rint model is not accurate enough to model highly dynamic profiles as the WLTC cycle.

4.5. Heat Generation Comparison ECMs

In this section, the breakdown of the heat generation as well as the comparison of the studied ECMs are described.

4.5.1. Heat Generation Breakdown

Depending on which ECMs are compared regarding their heat generation prediction, the breakdown between irreversible and reversible heat losses is relevant. ECMs using the same SOC-OCV data ($\mathrm{ECM}_{1-4,6-8}$) are expected to have identical reversible losses (neglecting minor temperature discrepancies). However, compared with different SOC starting points ($\mathrm{ECM}_{5,6}$), reversible heat losses can differ between the models. To capture this influence, firstly a breakdown between irreversible Joule losses Q_{irr} and reversible

entropic losses Q_{rev} for all three studied SOC points at ambient temperature $T_{amb} = 25\,^{\circ}\text{C}$ is performed.

The total heat generated over a WLTC is defined as

$$Q_{\text{WLTC}} = \sum_{t=0}^{t_{\text{end}}} Q(t) \tag{24}$$

which represents the sum of every generated heat per time step. Figure 9 (right) shows that the total generated heat Q_{tot} differs significantly between the start SOC points. The reason for that is more on the reversible term than on the irreversible one. While the irreversible heat generation Q_{irr} is in a range of 5% at all three SOC points, the reversible heat generation Q_{rev} is the main factor for the difference in the total generated heat. The root cause behind this is explained in Figure 4. While the entropic coefficient is negative (exothermic entropy reaction), the reversible heat term is positive. When the entropic coefficient is positive (endothermic entropy reaction) the reversible heat term is negative. Compared to the heat generation at SOC = 25%, the total heat generation over the WLTC cycle at SOC = 50% is 83% less, and at SOC = 75% it is 56% less.

With the gained knowledge over the heat generation breakdown, the results regarding the studied ECMs can be analyzed.
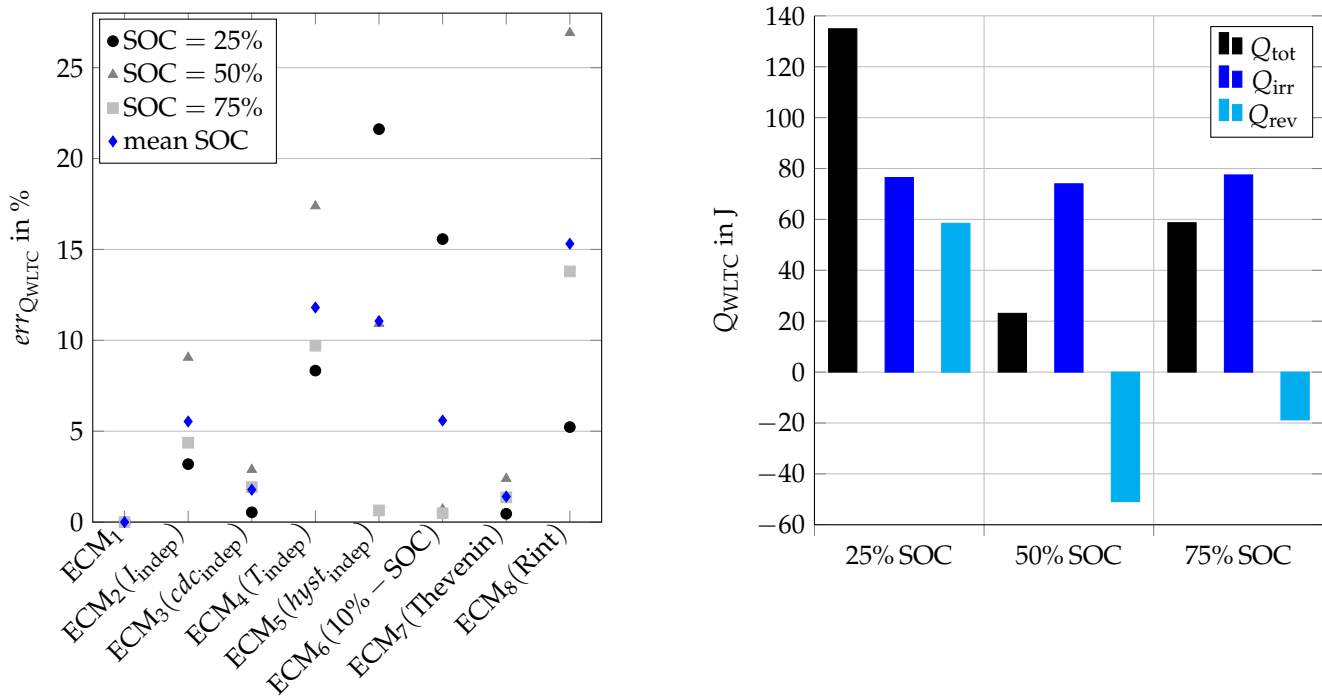

Figure 9. Left: Comparison of studied ECMs (error in reference to ECM_1) for the sum of generated heat over a WLTC cycle; **right**: total, irreversible and reversible heat generation breakdown at $T_{amb} = 25\,^{\circ}\text{C}$ and SOC $= 25, 50, 75\%$ for the ECM_1.

4.5.2. ECM Comparison

Since there are no experimentally measured heat generation rates available, the heat generation results of the ECM_1 model with all dependencies was set as reference. So, the error $err_{Q_{\text{WLTC}}}$ is defined as the absolute error value

$$err_{Q_{\text{WLTC}}} = \frac{|Q_{\text{WLTC}}(\text{ECM}_1) - Q_{\text{WLTC}}(\text{ECM}_i)|}{Q_{\text{WLTC}}(\text{ECM}_1)} \tag{25}$$

whereas $Q_{\text{WLTC}}(\text{ECM}_i)$ represents the heat generation of the compared ECM. Using the mean error per time step is not beneficial in this case, since the WLTC profile has time phases with an applied current of zero. This equals to no heat generation of the LIB and hence would distort the discussion. This enables this study to quantitatively analyze the influence of the studied parameter dependencies and architectures on the predicted generated heat. The assumption is valid, since the overall mean voltage error $err_{\text{U}} = 0.241\%$ of the ECM_1 is accurate to describe the battery voltage in highly dynamic drive cycles. The results are shown in Figure 9 (left).

The influence of the dependencies is discussed from left to right. The current independent ECM_2 has an mean SOC heat generation error of $err_{Q_{\text{WLTC}}} = 5.5\%$. Compared with the voltage difference to the ECM_1 of 1.2%, the influence on the predicted heat generation is increased by more than four times. The reason for this is the mean voltage error $err_{\text{U,mean}}$. The current dependency mainly has an influence on the voltage prediction at the current peaks. For the studied LIB the WLTC profile has only few high current peaks, as can be seen in Figure 6. However, in terms of the heat generation, the current peaks are responsible for the majority of the generated heat in the WLTC profile. In consequence, the current dependency is more important for the heat generation prediction than for the voltage prediction in highly dynamic drive cycles. For a better visualization of the results, the heat generation absolute error over time is shown in Appendix A Figure A4.

The charge/discharge pulse independent ECM_3 shows a heat generation average error of $err_{Q_{\text{WLTC}}} = 1.7\%$. Since it has no significant influence on neither the voltage nor the heat generation prediction, this dependency can be neglected.

The temperature independent ECM_4 results in an error of $err_{Q_{\text{WLTC}}} = 11.8\%$. While the error for all three SOC points at $T_{\text{amb}} = 25\,^{\circ}\text{C}$ is 0.28% in average, it increases to 5.5% at $T_{\text{amb}} = 35\,^{\circ}\text{C}$ and to 29.5% at $T_{\text{amb}} = 15\,^{\circ}\text{C}$. Hence, in accordance with the voltage prediction results, temperature should never be neglected either for the voltage or for the heat generation prediction.

The mean SOC heat generation error for the hysteresis independent ECM_5 is equal to $err_{Q_{\text{WLTC}}} = 11.1\%$. The main reason can be identified in the assumed SOC-correction, agreeing well with the conclusions of the voltage results. However, there are not only the increased LIB resistances. Regarding the heat generation, different start SOCs result in the usage of different entropic coefficient values. The importance of the entropic coefficient terms can be seen, because the error increases from 0.6% at SOC = 75%, to 10.9% at SOC = 50% and even 21.6% at SOC = 25%. Relating to Figure 4, the gradient of the entropic coefficient can be identified as the main cause for this observation. Hence, when relying on the predicted heat generation, the hysteresis effect has to be taken into account also for nickel manganese cobalt cells. The increasing heat generation error over time can additionally be seen in Appendix A Figure A5.

For the 10% SOC step model (ECM_6), the mean SOC heat generation error is at $err_{Q_{\text{WLTC}}} = 5.6\%$. This can be attributed to the same reasons as for the previously discussed ECM_5. Hence, 5% SOC steps should be used.

Finally, the ECM architecture influence is discussed. The Thevenin architecture has a mean SOC heat generation error of $err_{Q_{\text{WLTC}}} = 1.4\%$. This is within the limits of the accepted tolerance for the heat generation prediction. Analyzing the Rint architecture ECM_8, the error is at $err_{Q_{\text{WLTC}}} = 15.3\%$. The high discrepancy for the ECM_8 is explained by the insufficient modeling of the dynamic resistances of the LIB.

Taking the voltage and heat generation results into account, the most suitable ECM for thermal modeling simulations can be identified. Out of all studied parameters and architectures only one has been shown as neglectable in the voltage as well as in the heat generation comparison. The charge/discharge pulse dependency can be neglected in the voltage prediction (error to $\text{ECM}_1 = 0.6\%$) and in the heat generation prediction (error to $\text{ECM}_1 = 1.7\%$). All other dependencies and architectures result in one of the two predictions in mean errors > 5%. However, for thermal simulations the Thevenin ECM architecture has an error in the heat generation prediction of only 1.4% compared to the

ECM_1. Hence, because of the decreased computational effort the Thevenin model can be used for thermal management simulations, while for electrical simulation a DP model should be preferred.

To show the importance of the influence on heat generation prediction, the BEV of comparison is shortly explained. The chosen LIB for this study is comparable to the LIB cells used in the Tesla Model 3 Long Range. In total, there are 4416 cells in this BEV [43]. So, while the absolute heat generation error in Joule can seem small in the first place, by multiplying it by the total amount of cells, the heat generation prediction error can have a large impact on the design of thermal management systems. Assuming that the ECM_1 predicts the LIB heat generation perfectly well, for the WLTC cycle at $T_{amb} = 25\,°C$ and SOC = 25%, a 5.5% misprediction in the heat generation over the whole WLTC cycle would result in a total generated heat misprediction of $Q_{err,cell} = 7.42\,J$ for one cell and $Q_{err,Tesla-LIB-Pack} = 32.8\,kJ$ for 4416 LIB cells.

5. Conclusions

This paper describes a complete workflow for the characterization and parameter identification of ECMs for LIBs. Furthermore, different test procedures for the characterization of the OCV and the entropic coefficient have been studied and compared. Additionally, the developed parameter identification tool enables the user to study the influence of different ECM parameter dependencies and architectures. The LUTs generated by the tool have been used to compare the resulting ECMs regarding the voltage and heat generation prediction. The key results of this paper are summarized in the following.

The relaxation method results in a more accurate description of the OCV than the constant current method. The OCV method for the determination of the entropic coefficient delivers insufficient results. Hence, the RM method with the separate entropic coefficient test procedure should be used and justifies the additional test time. The resulting ECM_1 model with all dependencies shows good agreement with the validation experiments. The mean accuracy over all validation cycles is at 0.241% (8.77 mV) error in the voltage prediction.

Concluding the voltage and heat generation results, this study recommends using a Thevenin ECM with all parameter dependencies included except for the charge/discharge current dependency for the thermal modeling. Taking into account both the voltage and heat generation prediction changes the best suitable model compared to only considering the voltage prediction, whereas the neglection of hysteresis or current would be acceptable. If LIB parameters such as energy need to be considered as well, this study recommends using a DP model neglecting charge/discharge current dependency. The results help to better understand the influence of the chosen ECM on key parameters as voltage or heat generation and can save valuable computational effort for 1D/3D battery pack simulations for thermal management designers.

Further studies are planned to capture the LIB thermal properties over the studied temperature range and the heat generation over a WLTC and fast charge experimentally by using heat flux sensors. With those results, the models can again be compared regarding their heat generation prediction with the results of experimental data. The developed electro-thermal model will be used for LIB thermal management design studies and optimization.

Author Contributions: Conceptualization, M.A.; methodology, M.A and S.G.; software, M.A. and S.G.; validation, M.A.; formal analysis, M.A.; investigation, M.A.; resources, M.A. and T.K.; data curation, M.A.; writing—original draft preparation, M.A.; writing—review and editing, T.K.; visualization, M.A.; supervision, M.A., T.K. and A.W.; project administration, M.A., T.K. and A.W. All authors have read and agreed to the published version of the manuscript.

Data Availability Statement: The data that support the findings of this study are available from the corresponding author, M.A., upon reasonable request.

Conflicts of Interest: The authors declare no conflict of interest.

Nomenclature

Latin symbols

A	Area (m^2)
c_P	Specific Heat Capacity (J/kg K)
cdc	Charge/Discharge Pulse Dependency ($-$)
C	C-Rate Lithium-Ion-Battery ($-$)
C	Capacitance (F)
C_N	Nominal Capacity (A h)
d	Diameter (m)
err	Error (%)
h	Heat Transfer Coefficient (W/m^2 K)
$hyst$	Hysteresis Dependency ($-$)
I	Current (A)
k	Heat Conductivity (W/m K)
L	Length (m)
m	Mass (kg)
Nu	Nusselt Number ($-$)
Pr	Prandtl Number ($-$)
Q	Total Charge (A h)
Q	Heat (J)
$\dot{Q}$	Heat Generation Rate (W)
R	Electrial Resistance (Ω)
R_0	Ohmic Resistance (Ω)
Ra	Rayleigh Number ($-$)
SOC_0	Previous State of Charge ($-$)
t	Time (s)
T	Temperature (K)
U	Voltage (V)
V	Volume (m^3)

Greek Symbols

ϵ	Emissivity ($-$)
η_C	Coulombic Efficiency ($-$)
ρ	Density (kg m^{-3})
σ	Stefan-Boltzmann-Constant (W/m^2 K^4)
τ	Time Constant (s)

Subscripts

amb	Ambient
cell	Lithium-Ion-Battery Cell
conv	Heat Convection
exp	Experimentally
end	End Time
i	Counting Variable
indep	Independent
irr	Irreversible Losses
mean	Mean Error
mix	Mixing Enthalpy Losses
OCV	Open Circuit Voltage
pulse	Current Pulse
rad	Heat Radiation
reac	Side Reaction Losses
rel	Relaxation Time
rest	Rest Time
rev	Reversible Losses
t	Terminal Voltage

Abbreviations

BEV	Battery Electric Vehicle
CCM	Constant Current Test Method
DP	Dual Polarization Model
EC	Entropic Coefficient Test Method
ECM	Electrical Equivalent Circuit Model
EIS	Electrical Impedance Spectroscopy
HPPC	High Pulse Power Characterization
LIB	Lithium-Ion-Battery
LUT	Look-Up Tables
OCV	Open Circuit Voltage
RC	Resistance-Capacitance
RM	Relaxation Test Method
SOC	State Of Charge
SOH	State Of Health
WLTC	World Harmonized Light Vehicle Test Cycle

Appendix A
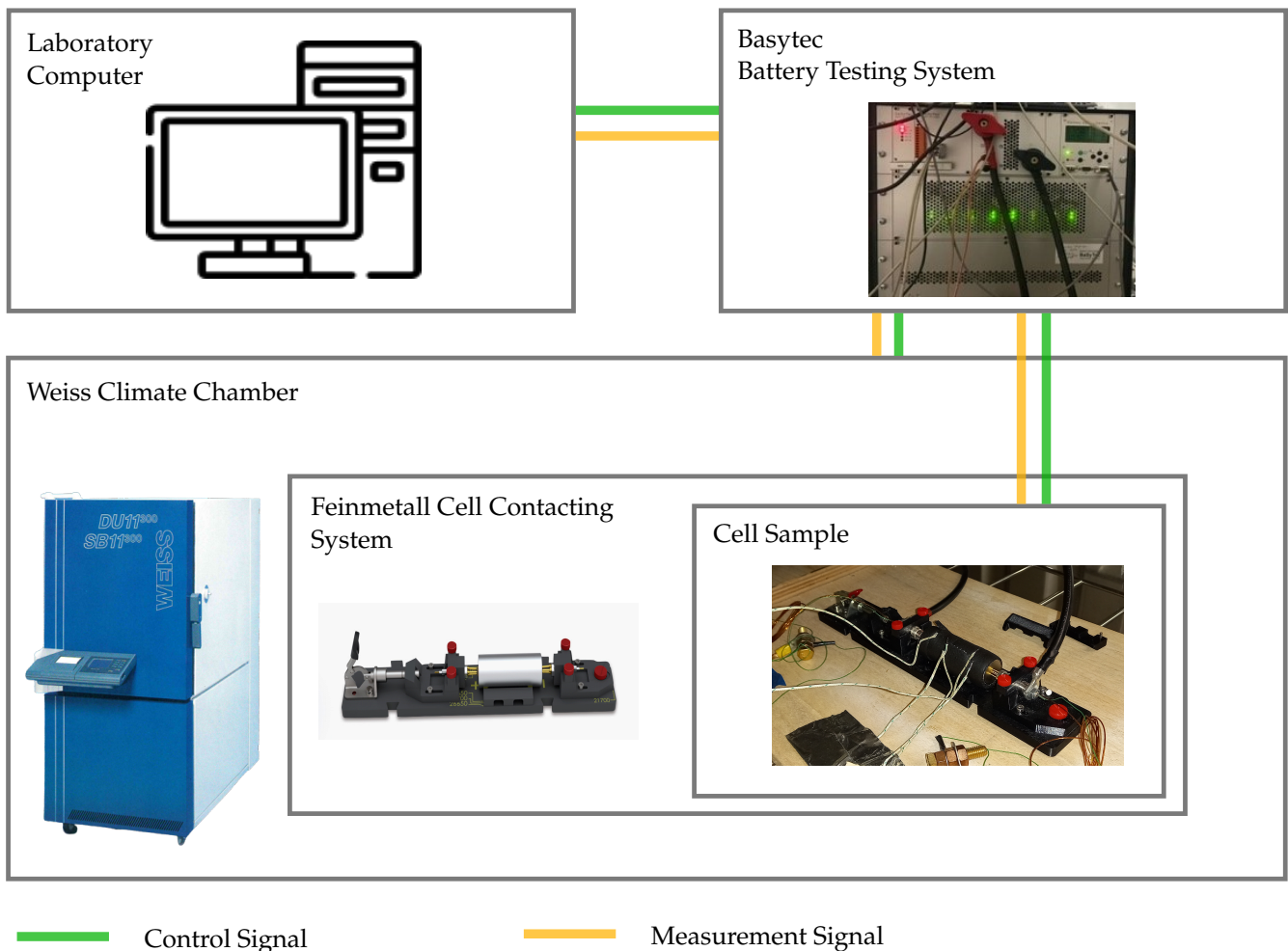
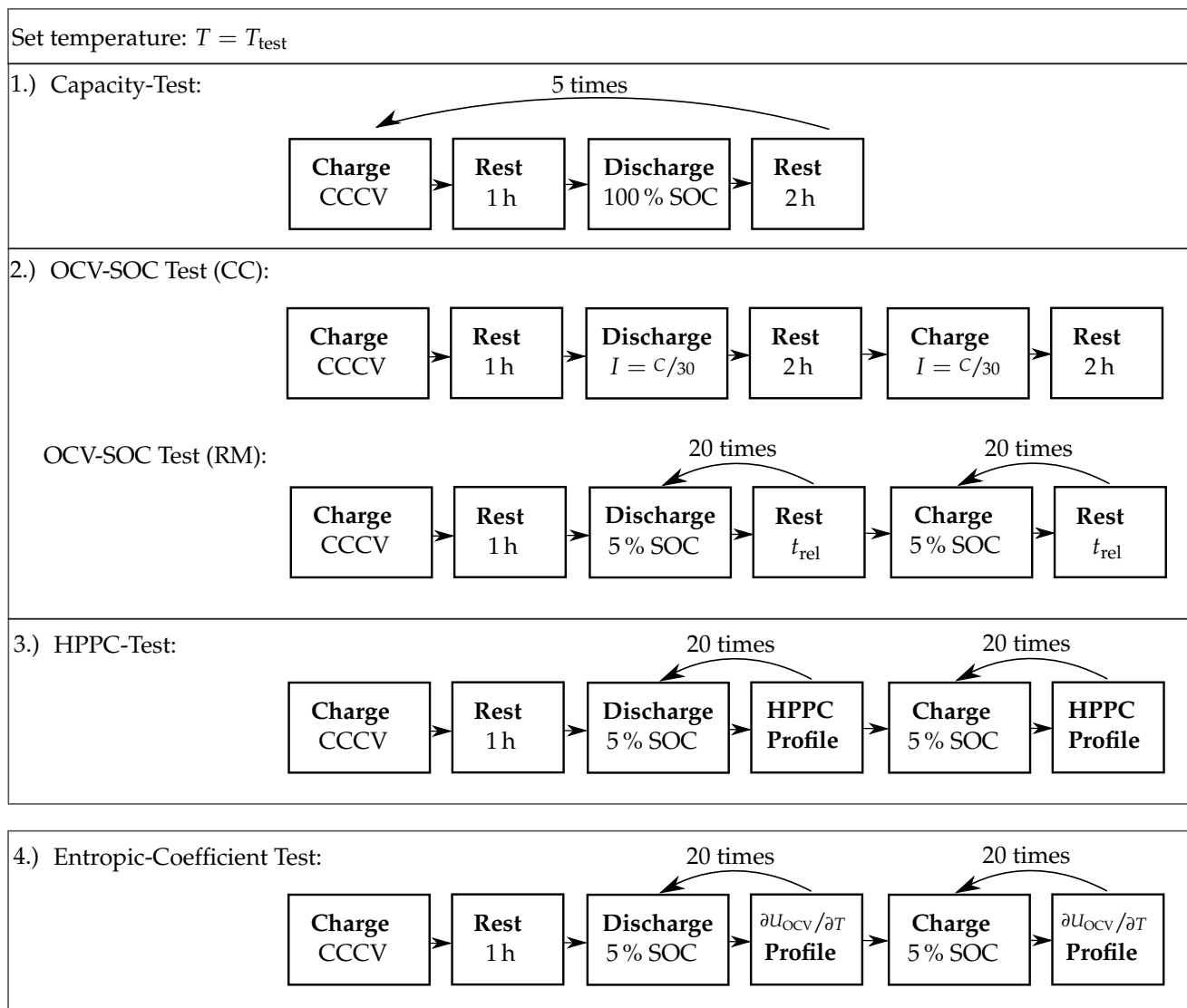**Figure A1.** Experimental platform of the Lithium-Ion-Battery (LIB) test bench.

Figure A2. Examined test procedure for the the LIB ECM characterization. Tests (1.)–(3.) need to be examined at all test temperatures, test (4.) only needs to be examined once.

Table A1. Comparison of experimental start SOC and simulation start SOC with OCV-SOC-correction.

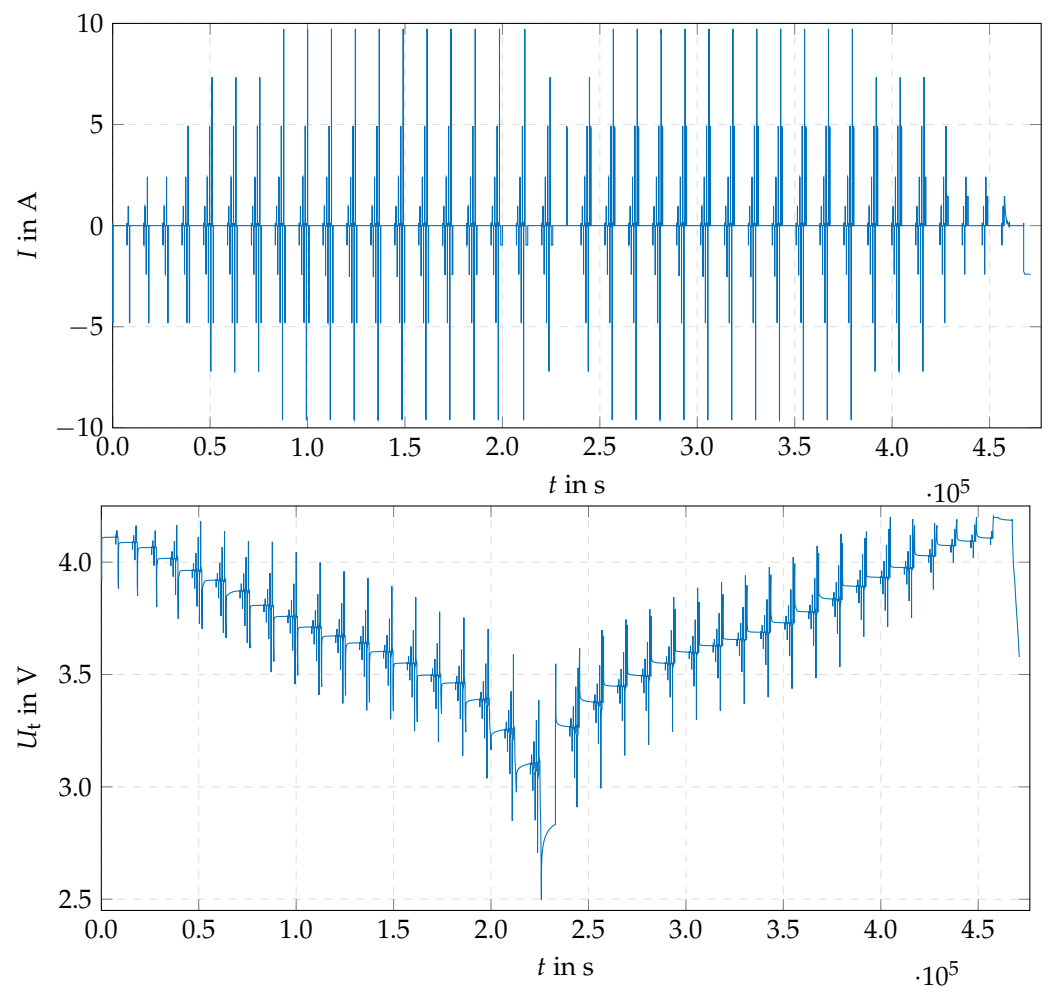| Temperature T_{amb} in °C	Experimental Start SOC	Start SOC ECM$_{1,2,3,7,8}$	Start SOC ECM$_4$	Start SOC ECM$_5$	Start SOC ECM$_6$
15	0.250	0.239	0.255	0.213	0.225
15	0.500	0.502	0.508	0.491	0.502
15	0.750	0.752	0.758	0.745	0.745
25	0.250	0.241	0.241	0.213	0.222
25	0.500	0.500	0.500	0.489	0.500
25	0.750	0.753	0.753	0.746	0.745
35	0.250	0.245	0.247	0.218	0.227
35	0.500	0.501	0.505	0.491	0.501
35	0.750	0.753	0.755	0.747	0.746

Figure A3. High Pulse Power Characterization (HPPC) current (**top**) and voltage (**bottom**) results using 5% SOC-steps for discharge and charge at $T_{amb} = 25\,°\text{C}$.
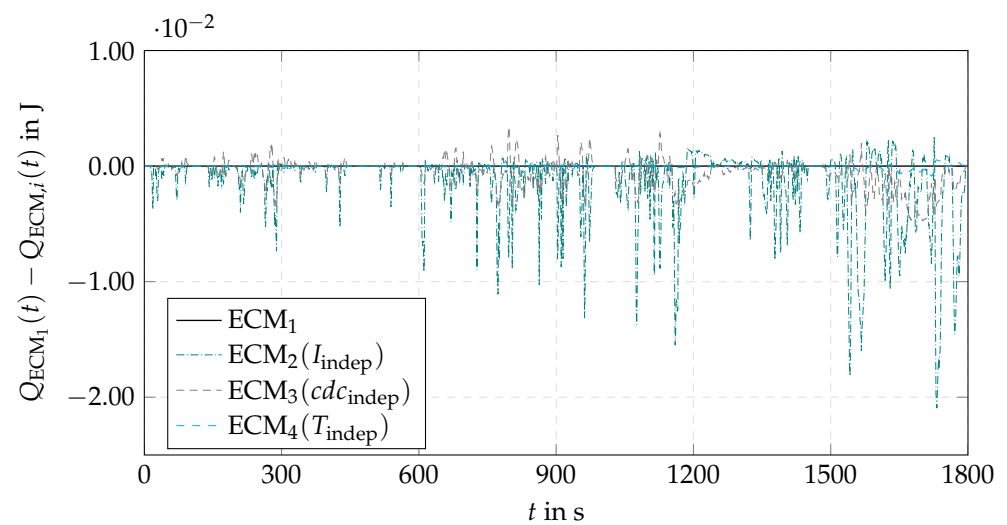

Figure A4. Comparison of heat generation prediction over the WLTC cycle at $T_{amb} = 25\,°\text{C}$ and SOC = 50%.
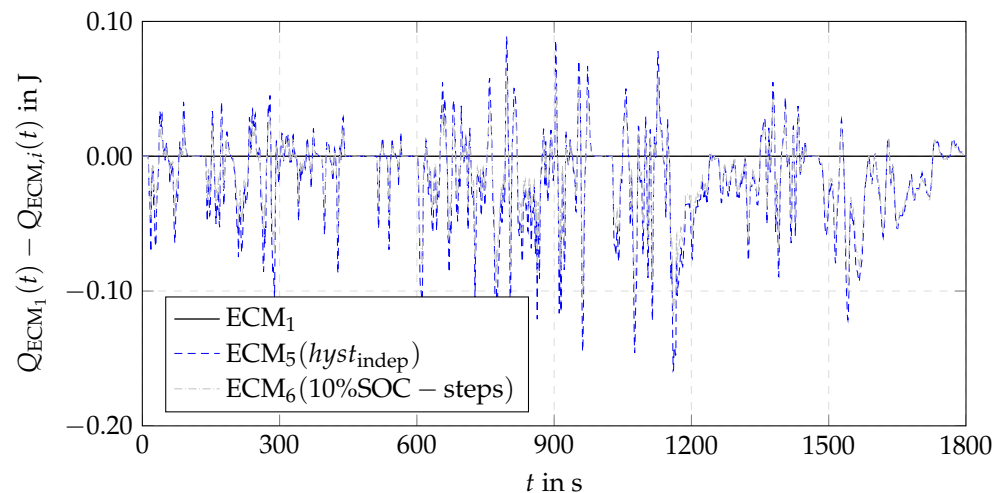
Figure A5. Comparison of heat generation prediction over the WLTC cycle at $T_{\mathrm{amb}} = 25\,°\mathrm{C}$ and SOC = 25%.

References

1. European Union. Fit for 55. 2022. Available online: https://www.bundesregierung.de/breg-de/themen/europa/fit-for-55-eu-1 942402 (accessed on 18 October 2022).
2. Jouhara, H.; Khordehgah, N.; Serey, N.; Almahmoud, S.; Lester, S.P.; Machen, D.; Wrobel, L. Applications and thermal management of rechargeable batteries for industrial applications. *Energy* **2019**, *170*, 849–861. [CrossRef]
3. Liu, J.; Duan, Q.; Ma, M.; Zhao, C.; Sun, J.; Wang, Q. Aging mechanisms and thermal stability of aged commercial 18650 lithium ion battery induced by slight overcharging cycling. *J. Power Sources* **2020**, *445*, 227263. [CrossRef]
4. Hussein, A.A. Experimental modeling and analysis of lithium-ion battery temperature dependence. In Proceedings of the 2015 IEEE Applied Power Electronics Conference and Exposition (APEC), Charlotte, NC, USA, 15–19 March 2015; pp. 1084–1088.
5. Waldmann, T.; Wilka, M.; Kasper, M.; Fleischhammer, M.; Wohlfahrt-Mehrens, M. Temperature dependent ageing mechanisms in Lithium-ion batteries—A Post-Mortem study. *J. Power Sources* **2014**, *262*, 129–135. [CrossRef]
6. Lu, Z.; Yu, X.; Wei, L.; Cao, F.; Zhang, L.; Meng, X.; Jin, L. A comprehensive experimental study on temperature-dependent performance of lithium-ion battery. *Appl. Therm. Eng.* **2019**, *158*, 113800. [CrossRef]
7. Pesaran, A.A. Battery thermal models for hybrid vehicle simulations. *J. Power Sources* **2002**, *110*, 377–382. [CrossRef]
8. Plett, G.L. *Battery Management Systems, Volume I: Battery Modeling*; Artech House: Norwood, MA, USA, 2015.
9. Nejad, S.; Gladwin, D.; Stone, D. A systematic review of lumped-parameter equivalent circuit models for real-time estimation of lithium-ion battery states. *J. Power Sources* **2016**, *316*, 183–196. [CrossRef]
10. Wang, Q.K.; He, Y.J.; Shen, J.N.; Ma, Z.F.; Zhong, G.B. A unified modeling framework for lithium-ion batteries: An artificial neural network based thermal coupled equivalent circuit model approach. *Energy* **2017**, *138*, 118–132. [CrossRef]
11. Zhang, X.; Zhang, W.; Lei, G. A review of li-ion battery equivalent circuit models. *Trans. Electr. Electron. Mater.* **2016**, *17*, 311–316. [CrossRef]
12. Bernardi, D.; Pawlikowski, E.; Newman, J. A general energy balance for battery systems. *J. Electrochem. Soc.* **1985**, *132*, 5. [CrossRef]
13. Wildfeuer, L.; Wassiliadis, N.; Reiter, C.; Baumann, M.; Lienkamp, M. Experimental characterization of Li-ion battery resistance at the cell, module and pack level. In Proceedings of the 2019 Fourteenth International Conference on Ecological Vehicles and Renewable Energies (EVER), Monte-Carlo, Monaco, 8–10 May 2019; pp. 1–12.
14. Behi, H.; Karimi, D.; Jaguemont, J.; Gandoman, F.H.; Kalogiannis, T.; Berecibar, M.; Van Mierlo, J. Novel thermal management methods to improve the performance of the Li-ion batteries in high discharge current applications. *Energy* **2021**, *224*, 120165. [CrossRef]
15. Liang, Z.; Wang, R.; Malt, A.H.; Souri, M.; Esfahani, M.; Jabbari, M. Systematic evaluation of a flat-heat-pipe-based thermal management: Cell-to-cell variations and battery ageing. *Appl. Therm. Eng.* **2021**, *192*, 116934. [CrossRef]
16. Alihosseini, A.; Shafaee, M. Experimental study and numerical simulation of a Lithium-ion battery thermal management system using a heat pipe. *J. Energy Storage* **2021**, *39*, 102616. [CrossRef]
17. Qian, Z.; Li, Y.; Rao, Z. Thermal performance of lithium-ion battery thermal management system by using mini-channel cooling. *Energy Convers. Manag.* **2016**, *126*, 622–631. [CrossRef]
18. Cao, R.; Zhang, X.; Yang, H. Prediction of the Heat Generation Rate of Lithium-Ion Batteries Based on Three Machine Learning Algorithms. *Batteries* **2023**, *9*, 165. [CrossRef]
19. Pang, H.; Wu, L.; Liu, J.; Liu, X.; Liu, K. Physics-informed neural network approach for heat generation rate estimation of lithium-ion battery under various driving conditions. *J. Energy Chem.* **2023**, *78*, 1–12. [CrossRef]

20. Wu, L.; Liu, K.; Liu, J.; Pang, H. Evaluating the heat generation characteristics of cylindrical lithium-ion battery considering the discharge rates and N/P ratio. *J. Energy Storage* **2023**, *64*, 107182. [CrossRef]

21. Liu, J.; Huang, Z.; Sun, J.; Wang, Q. Heat generation and thermal runaway of lithium-ion battery induced by slight overcharging cycling. *J. Power Sources* **2022**, *526*, 231136. [CrossRef]

22. Catenaro, E.; Onori, S. Experimental data of lithium-ion batteries under galvanostatic discharge tests at different rates and temperatures of operation. *Data Brief* **2021**, *35*, 106894. [CrossRef]

23. Kim, Y.S. Product Specifications Rechargeable Lithium Ion Battery Model: INR21700 M50 18.20Wh. 2016. Available online: https://www.dnkpower.com/wp-content/uploads/2019/02/LG-INR21700-M50-Datasheet.pdf (accessed on 18 October 2022).

24. He, H.; Xiong, R.; Fan, J. Evaluation of lithium-ion battery equivalent circuit models for state of charge estimation by an experimental approach. *Energies* **2011**, *4*, 582–598. [CrossRef]

25. Hu, X.; Li, S.; Peng, H. A comparative study of equivalent circuit models for Li-ion batteries. *J. Power Sources* **2012**, *198*, 359–367. [CrossRef]

26. Ng, K.S.; Moo, C.S.; Chen, Y.P.; Hsieh, Y.C. Enhanced coulomb counting method for estimating state-of-charge and state-of-health of lithium-ion batteries. *Appl. Energy* **2009**, *86*, 1506–1511. [CrossRef]

27. Spotnitz, R.; Franklin, J. Abuse behavior of high-power, lithium-ion cells. *J. Power Sources* **2003**, *113*, 81–100. [CrossRef]

28. Thomas, K.E.; Newman, J. Thermal modeling of porous insertion electrodes. *J. Electrochem. Soc.* **2003**, *150*, A176. [CrossRef]

29. Siemens, P. *STAR-CCM+ User Guide Version 13.04*; Siemens PLM Software Inc.: Munich, Germany, 2022.

30. Immonen, E.; Hurri, J. Incremental thermo-electric CFD modeling of a high-energy Lithium-Titanate Oxide battery cell in different temperatures: A comparative study. *Appl. Therm. Eng.* **2021**, *197*, 117260. [CrossRef]

31. Klan, H. Wärmeübergang durch freie Konvektion an umströmten Körpern. In *VDI-Wärmeatlas*; Springer: Berlin/Heidelberg, Germany, 2002; pp. 567–591.

32. Stephan, P. B2 Grundlagen der Berechnungsmethoden für Wärmeleitung, konvektiven Wärmeübergang und Wärmestrahlung. In *VDI-Wärmeatlas*; Springer: Berlin/Heidelberg, Germany, 2019; pp. 23–36.

33. Basytec. Battery Cell and Module Test System, 2017. Available online: https://basytec.de/prospekte/2023_01_BaSyTec%20MRS.pdf (accessed on 18 October 2022).

34. Nikolian, A.; Jaguemont, J.; De Hoog, J.; Goutam, S.; Omar, N.; Van Den Bossche, P.; Van Mierlo, J. Complete cell-level lithium-ion electrical ECM model for different chemistries (NMC, LFP, LTO) and temperatures (-5 C to 45 C)–Optimized modelling techniques. *Int. J. Electr. Power Energy Syst.* **2018**, *98*, 133–146. [CrossRef]

35. Belt, J.R. *Battery Test Manual for Plug-in Hybrid Electric Vehicles*; Technical Report; Idaho National Lab. (INL): Idaho Falls, ID, USA, 2010.

36. Schmidt, J.P. *Verfahren zur Charakterisierung und Modellierung von Lithium-Ionen Zellen*; KIT Scientific Publishing: Karlsruhe, Germany, 2013; Volume 25.

37. Geifes, F.; Bolsinger, C.; Mielcarek, P.; Birke, K.P. Determination of the entropic heat coefficient in a simple electro-thermal lithium-ion cell model with pulse relaxation measurements and least squares algorithm. *J. Power Sources* **2019**, *419*, 148–154. [CrossRef]

38. Forgez, C.; Do, D.V.; Friedrich, G.; Morcrette, M.; Delacourt, C. Thermal modeling of a cylindrical LiFePO4/graphite lithium-ion battery. *J. Power Sources* **2010**, *195*, 2961–2968. [CrossRef]

39. Zhu, Q.; Xiong, N.; Yang, M.L.; Huang, R.S.; Hu, G.D. State of charge estimation for lithium-ion battery based on nonlinear observer: An H_∞ method. *Energies* **2017**, *10*, 679. [CrossRef]

40. Geng, Z.; Groot, J.; Thiringer, T. A time-and cost-effective method for entropic coefficient determination of a large commercial battery cell. *IEEE Trans. Transp. Electrif.* **2020**, *6*, 257–266. [CrossRef]

41. Steinhardt, M.; Gillich, E.I.; Rheinfeld, A.; Kraft, L.; Spielbauer, M.; Bohlen, O.; Jossen, A. Low-effort determination of heat capacity and thermal conductivity for cylindrical 18650 and 21700 lithium-ion cells. *J. Energy Storage* **2021**, *42*, 103065. [CrossRef]

42. Bui, T.M.; Niri, M.F.; Worwood, D.; Dinh, T.Q.; Marco, J. An Advanced Hardware-in-the-Loop Battery Simulation Platform for the Experimental Testing of Battery Management System. In Proceedings of the 2019 23rd International Conference on Mechatronics Technology (ICMT), Salerno, Italy, 23–26 October 2019; pp. 1–6.

43. Lambert, F. Tesla Model 3: Exclusive First Look at Tesla's New Battery Pack Architecture. 2017. Available online: https://electrek.co/2017/08/24/tesla-model-3-exclusive-battery-pack-architecture/ (accessed on 18 October 2022).